Journal of Quantitative Spectroscopy & Radiative Transfer 254 (2020) 107184

Contents lists available at ScienceDirect

Journal of Quantitative Spectroscopy & Radiative Transfer

journal homepage: www.elsevier.com/locate/jqsrt

Three-dimensional tomography reveals distinct morphological and optical properties of soot aggregates from coal-fired residential stoves in China

Chenchong Zhang [a], William R. Heinson [a], Pai Liu [a], Payton Beeler [a], Qing Li [b], Jingkun Jiang [c], Rajan K. Chakrabarty [a,d,*]

[a] Center for Aerosol Science and Engineering, Department of Energy, Environmental and Chemical Engineering, Washington University in St. Louis, St. Louis, MO 63130, USA
[b] Shanghai Key Laboratory of Atmospheric Particle Pollution and Prevention, Department of Environmental Science and Engineering, Institute of Atmospheric Sciences, Fudan University, Shanghai, 200433, China
[c] State Key Joint Laboratory of Environment Simulation and Pollution Control, School of Environment, Tsinghua University, Beijing, 100084, China
[d] McDonnell Center for the Space Sciences, Washington University in St. Louis, St. Louis, MO 63130, USA

A R T I C L E I N F O

Article history:
Received 16 January 2020
Revised 14 May 2020
Accepted 22 June 2020
Available online 23 June 2020

A B S T R A C T

Electron tomography (ET) is used to reconstruct the exact 3-dimensional morphologies of fractal-like soot aggregates sampled from a household heating stove commonly used in China. Conventional ET techniques suffer from “the missing wedge” problem caused by unreachable tilt angles, leading to noisy reconstructed tomograms. We overcame this problem by implementing a high-resolution object-edge identification method coupled with a novel voxel-filling algorithm to improve the reconstruction quality. Our reconstructed micron-length aggregates highlight the local non-idealities present throughout a particle’s surface; these characteristics are almost impossible to account for in existing computational simulation exercises. Q-space analysis predicts the fractal dimension of our ET reconstructed aggregates to be in the range between 2.2 and 2.6, which deviates significantly from the universal value of 1.8 obtained using the widely adopted diffusion limited cluster-cluster aggregation (DLCA) model. The optical properties of our ET reconstructed aggregates are compared with those built with a DLCA model and equivalent spheres . The most striking optical characteristics of the ET reconstructed aggregates are their wavelength invariant mass absorption cross-sections of ~3.5 m^2/g and single scattering albedo of ~0.5. The sample size investigated in this work is constrained by the extremely time-consuming object-edge identification process of electron tomography. This issue necessitates the development of more efficient computer vision algorithms for future research.

1. Introduction

Residential coal combustion is a primary source of heating and cooking in rural areas of developing countries such as China and India [1–3]. Incomplete coal combustion in household stoves produces soot, which accounts for a large fraction of the regional carbonaceous aerosol emissions [4,5]. Soot particles strongly scatter and absorb solar radiation and are consequentially recognized as an important climate forcer [6,7]. The optical properties of soot, which are crucial to radiative forcing estimations, depend highly on the complex fractal-like morphology of soot aggregates [8,9]. Thus, an accurate parameterization of soot morphology is a prerequisite to constraining the uncertainties in the estimates of Earth’s energy balance and thereby advancing the currently adopted climate model.

The morphology of soot aggregates is most commonly characterized with *ex situ* electron microscopy (EM) and subsequent digital image analysis [10,11]. This technique requires experimentalists to extract the unknown three-dimensional (3-d) geometric characteristics of soot aggregates from their two-dimensional (2-d) projected images, according to certain shape approximation assumptions or experimentally-determined correction factors [10,12,13]. Since soot aggregates possess anisotropic shapes [14,15], an inference of their 3-d morphology (from 2-d projected images) is inevitably subject to the random orientations by which aggregates reside on the EM grids. Previous studies [16,17] show that the

* Corresponding author
E-mail address: chakrabarty@wustl.edu (R.K. Chakrabarty).

https://doi.org/10.1016/j.jqsrt.2020.107184
0022-4073/© 2020 Published by Elsevier Ltd.

key morphological parameters of a soot particle (such as monomer number, projected area, and fractal dimension D_f) inferred from EM images taken from multiple angles deviate significantly with each other [18,19].

Alternatively, the 3-d morphology of aggregates can be studied with computer simulations based on Monte Carlo method, for example, the diffusion limited cluster-cluster aggregation (DLCA) model, which mimics the dynamic process of soot aggregates growth in stochastic Brownian systems [15,20,21]. Such a model generates 3-d "virtual aggregates" taking fractal shape, which are regarded as an approximation to the geometry of real-world soot. Subsequent analyses can be performed on the virtual aggregates to acquire their 3-d morphological parameters [22]. The use of computer simulation circumvents the projection artefacts in traditional EM analysis, but the idealized aggregate geometry, which is commonly assumed in simulation models, fails to capture the diversity in the minor structures of real-world soot [23]. For example, a DLCA model commonly treats soot monomers as equally sized and point-contacting spheres [20,21,24,25]. Only a few studies to our knowledge have considered the sintering induced intermonomer necking [26,27], the lognormal distribution of monomer radii [28], and the possible deviation of monomers from perfect spheres [23,29]. Furthermore, it is commonly assumed in simulations that the relative position of monomers in an aggregate remains unchanged once the monomers are joined together [21,24,25]. This is again not always true in real world scenarios. Recent experiments [18] provide evidence suggesting that the restructuring of soot aggregates (i.e. rotation per monomer contacting points) could occur simultaneously during their growth. Such a non-ideal overall structure of soot aggregates may also affect their optical properties in an unanticipated manner, which remains unaddressed in contemporary models.

The limitations of traditional EM techniques and computer simulations can be overcome with the advent of electron tomography (ET), by which experimentalists could characterize the 3-d morphology accurately. As a development of the transmission electron microscopy (TEM) method, ET is a powerful technique that captures 3-d nanoscale structures through multiple viewing-angle projections [18,30,31]. Doing so, the non-ideal structures of soot aggregates can be faithfully preserved in 3-d reconstruction from projection artefacts. In this study, we apply ET to reconstruct the complete 3-d geometry of soot aggregates sampled from residential heating stove, and subsequently we compute their optical properties based on the reconstructed geometries. This paper is organized as follows: First we briefly recap the theoretical foundation of the q-space analysis [32] and discrete dipole approximation (DDA) [32–34], which are respectively adopted here to compute the aggregates' morphological and optical parameters. Next, we describe the experimental methods involved in soot sampling and ET reconstruction. This is followed by section detailing a novel object-edge identification method (along with a voxel filling algorithm), which is designed to overcome the "the missing wedge [35,36]" problem inherent to ET, thereby improving the accuracy of final 3-d reconstruction. Next, we present the reconstructed 3-d geometry of soot aggregates, along with their morphological and optical parameters, which are respectively determined with q-space analysis and DDA. This paper concludes with a side-by-side comparison between the ET reconstructed soot and idealized DLCA aggregates, regarding their morphology and optical properties.

2. Theory

2.1. Q-space analysis of aggregate morphology

Q-space analysis has been widely adopted to study the morphology of aggregates [32,37]. This technique, which originates from light scattering experiments, involves plotting the structure factor (S, normalized scattering intensity) of the aggregate versus the magnitude of scattering wave vector q in a log-log space. The magnitude of $S(q)$ scales with q by a power-law exponent taking values of $-2D_m + D_s$ (where D_m and D_s respectively denote mass and surface dimension of the object). For fractal aggregates, $D_f = D_m = D_s$, the power-law scaling relationship is reduced to $S(q) \propto q^{-D_f}$. Thus, the size delimited fractal morphology along with the corresponding D_f values can be readily determined with $S(q)$ trends in the log-log space. In theoretical studies, one could calculate $S(q)$ according to the discrete form of the orientational averaged scattering intensity:

$$S(q) = \left| \frac{1}{N} \sum_{j=1}^{N} \exp\left[i\left(\vec{r_j} \cdot \vec{q} \right) \right] \right|^2, \quad \text{with } q = \frac{4\pi}{\lambda} \sin\left(\frac{\theta}{2} \right) \tag{1}$$

Here, N represents the number of point scatterers constituting the aggregates, $\vec{r_j}$ is the location of scatterer j relative to the origin, λ is the wavelength of the incident light, and θ is the scattering angle.

2.2. Discrete dipole approximation

The exact solution to electromagnetism equations are available only for objects with a symmetric geometry. For asymmetric objects, numerical approximation models are widely used to simulate the related optical properties. DDA is one of such model. DDA assumes the particle of interest is assembled by numerous dipoles. Each dipole, j, located at r_j from the coordinate origin, is illuminated by both the electric field, E_{incj}, due to the incident wave, and the radiation scattered by all the other oscillating dipoles, $E_{rad,\,k\neq j}$. The moment of dipole j, P_j, can be expressed as the product of the dipole polarizability, α_j, and the total external radiations:

$$P_j = \alpha_j \left(E_{inc,j} - E_{rad,k\neq j} \right) \quad (j = 1, 2, \ldots, N). \tag{2}$$

The monochromatic incident plane wave, E_0, polarized in two mutually orthogonal directions, propagates along vector k. The induced electric field, $E_{inc,j}$, can be written in a complex expression:

$$E_{inc,k} = E_0 \exp\left(ik \cdot r_k - i\omega t \right). \tag{3}$$

Meanwhile, for any dipole j, $E_{rad,j}$ is a linear combination of all the other dipole moments $P_{l\neq j}$. Therefore Eq. (2) can be compactly formulated as a set of N inhomogeneous linear complex vector equations of the form P_j (j = 1, 2, …, N) [33,38].

3. Methods

3.1. Soot sampling

Particle samples were collected from a widely used traditional heating stove (NS18-17, 18 kW, Beijing Laowan Bioenergy Technology Co., Ltd, China) in a rural Chinese household (see Fig. 1 for the schematic of sampling experiment). The stove with a dimension of 460 × 410 × 985 mm was placed at the center of a sealed room (about 10 m^3) maintained at a slightly positive pressure with filtered air. The flue gas from the stove was drawn out at a fixed flow rate of 0.56 m^3/s through a circular hood connected to a dilution tunnel. Locally available bituminous coal chunks were crushed into pieces of approximately 3 inches in diameter before being fed into the upper region of the stove combustion chamber, where they are ignited with a mixture of air and propane gas applied at a fixed

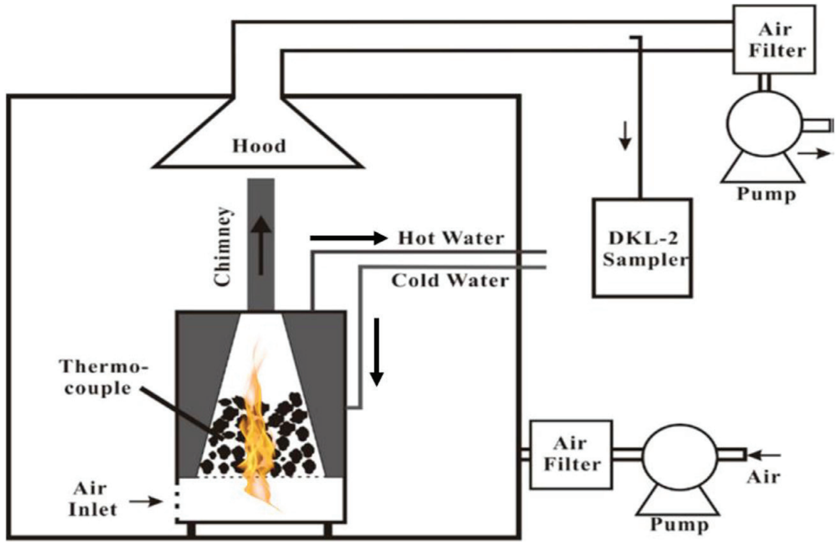

Fig 1. Schematic diagram of the experimental setup for soot particle sampling from a coal-combustion stove.

flow rate of 3 lpm. The stove design and its operation during the experiment are detailed in a previous publication [39].

Soot aggregates emitted from the stove were collected 4 meters downstream of the exhaust on carbon-coated copper TEM grids (300-mesh, Beijing XXBR Technology Co., Ltd, China) mounted on a DKL-2 type single-stage cascade impactor (0.5-mm-diameter jet nozzle). The flow rate of the impactor was set to 1 lpm. A sampling time of 20 seconds (determined in a trial-and-error manner) was used to ensure sufficient but not overcrowded loading of particles onto the grids [40]. We started TEM sampling about 30 min after ignition, at which a steady flaming condition was reached. Such a condition ensured that the sampled particles were produced from the combustion of coal, but not the propane pilot flame.

3.2. Electron tomography

We used a FEI Tecnai F20 TEM D545 microscope to acquire 2-d tilt-series of TEM images for four soot particles (hereafter sample A, B, C, and D). The ranges of title angles used for sample A, B, C, and D are respectively [− 60°, + 60°], [− 60°, + 70°], [− 60°, + 60°], and [− 65°, + 60°]. The title angle was incremented by one degree during the imaging. ET reconstruction was implemented through the weighted back projection algorithm in IMOD 4.9 coupled with the RAPTOR alignment module [41,42]. The reconstructed results are stacks of what we call "tomograms". Since 3-d ET reconstruction suffers from "the missing wedge" caused by unreachable tilt angles, the tomograms of the soot aggregate are normally noisy. In this study, we identified the boundary of soot particle from the reconstructed slices at the pixel locations where sharp contrast (between particle and background) is observed. These boundaries were determined in each slice, and when stacked together, constitute the closed surface of soot aggregate.

3.3. Voxel filling

Tomograms are made up of volumetric pixels (hereafter voxels) that represent the elementary geometric unit of a 3-d objects. An accurate voxel filling process (voxelization) is therefore fundamental to every subsequent analysis. In this work, we developed a layer-by-layer voxelization method to fill the space encapsulated by the aggregate surface.

Given the irregular fractal-like shape of soot aggregates, the most straightforward and effective voxelization procedure is to allocate voxels along successive horizontal lines in each tomogram slice. But this poses another challenge: the intersection points (hereafter IPs) between closed surface contours and the horizontal lines must be correctly identified as either starting or ending points for voxelization. Please refer to Fig. 2 for examples of IPs on a horizontal line in one tomogram slice.

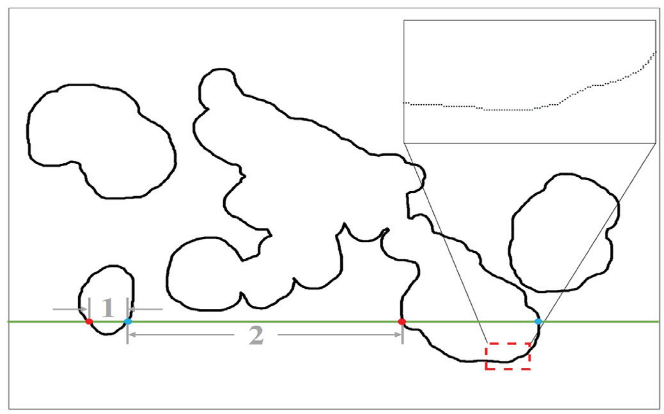

Fig. 2. An example of voxel filling in one tomogram slice. The inset shows the zoomed in view corresponding to the red-dashed square area. It highlights the continuous black points constituting the object boundaries The green line is one of the horizontal voxel filling lines (the filling direction in each horizontal line is from left to right). It has four intersection points (IPs). Voxel filling starts from the red points (voxel-filling starting points) and ends at the closest blue points (voxel-filling ending points). If the blue point on the left is the current IP, the number of pixels of "gap 1" is defined as the intra-prior distance (IPrD), and the number of pixels of "gap 2" is defined as the intra-posterior distance (IPoD).

We applied an intra-line and inter-line method to categorize IPs. We define the number of voxels between the current IP and the previous IP in each horizontal line as the intra-prior distance (IPrD), and the number of voxels between the next IP and the current IP as the intra-posterior distance (IPoD). For intra-line analysis, different value combinations of IPrD and IPoD help us to confirm the basic type of a given IP. In this study, basic types include boundary starting points (IPrD > 1 meanwhile IPoD = 1), boundary ending points (IPrD = 1 meanwhile IPoD > 1), singular boundary points (IPrD > 1 meanwhile IPoD > 1), and normal boundary points (IPrD = IPoD = 1). The first three types of boundary points are all possible starting or ending IPs for voxel filling.

Note that an intra-line analysis does not provide us a sufficient condition to determine whether the gap between two successive

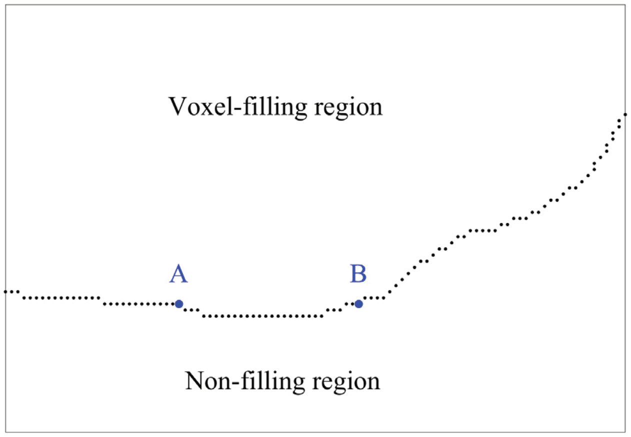

Fig. 3. The same figure as the inset of Figure 2. Here we highlight an example of an ambiguous case after intra-line categorization. The area above the black dots is the object region, which should be filled with voxels. The area below the black dots is the background region, which should be left blank. Both point A and point B are categorized as boundary ending points by intra-line analysis as introduced above. But point A is a voxel-filling starting point at the same time, while point B acts only as a voxel-filling ending point.

IPs should be voxelized. Curvatures of aggregate boundaries cause ambiguities to IPs categorizations. For example, a boundary ending point (Point A in Fig. 3) also represents a starting point for the subsequent voxel filling process. However, this is not the case for another boundary ending point (B in Fig. 3). Intra-line categorization thus cannot inform us whether we should start the voxel filling procedure at these points.

Here inter-line analysis aids in for finer categorization. We incorporate prior knowledge to distinguish, for example, whether a boundary ending point is a filling starting point or not. The principle we follow is that natural objects, e.g., soot aggregates in this study, should have continuous surfaces. In the voxel filling process, this principle can be interpreted as that successive horizontal lines (in either the bottom up or top down direction) should contain similar numbers of voxels after voxelization. Besides, a pair of starting and ending points for voxelization should locate in the region adjacent to their counterparts in the previous horizontal line. Given that the first horizontal filling line of each slice is always tangential to the object boundaries, intra-line analysis can categorize all the necessary filling starting and ending pairs accurately. Subsequently IP pairs in next horizontal lines can be accurately identified according to a combination of intra- and inter-line analysis.

3.4. Q-space analysis

Q-space analysis was next performed on the 3-d reconstructions of aggregates. We calculated of $S(q)$ according to Eq. (1), wherein the $\vec{r}$ was determined with the 3-d coordinates of voxels. In this treatment, the voxels making up the reconstructed aggregates are regarded as the point scatterers in q-space analysis [43,44].

3.5. Computation of optical properties

The optical properties of the ET reconstructed and DLCA aggregates are calculated with DDA. We compiled and ran DDSCAT 7.3.2 on a research computing cluster at Washington University in St. Louis equipped with a gfortran compiler. Isotropic polarizability was assigned to all voxels of the reconstructed aggregates. Related optical properties were simulated through appropriate numbers of dipole representations of each aggregate model. A convergence test of the DDA simulation is detailed in supplementary information (Figure S2).

4. Results and discussion

4.1. Reconstruction of aggregate geometry in 3-d

Fig. 4 shows snapshots of the ET reconstructed aggregates. One could observe that the detailed non-ideal morphologies of soot monomers, such as the intermonomer necking and the deviation of monomers from spherical shape, are faithfully preserved in the 3-d reconstruction. Furthermore, the non-ideal overall structure of the aggregate backbone can be observed in the reconstruction of aggregate C, for example, the internal ring structure due to the possible restructuring of the aggregate during its growth [45]. We also notice that, except for aggregate D wherein two extremely large monomers are observed, the other three aggregates are comprised of monomers of similar size. This monodisperse distribution of monomer radii implies that the nascent soot particles experience similar combustion and transport conditions. For aggregate D, the two extremely large monomers have similar pixel values as the other smaller monomers in the projection images. It is reasonable to recognize them as consisting of identical black carbon components with those smaller counterparts.

4.2. Q-space analysis

Here, we compare the morphological parameters of ET reconstructed aggregates to that of idealized DLCA aggregates. The number of constituent monomers in the DLCA aggregates ranges between 50 and 150, ensuring that the DLCA are of the comparable size relative to the ET reconstrued ones. Fig. 5 shows the q-space analysis of all four ET reconstructed aggregates and a typical DLCA aggregate. Here we plot the normalized structure factor $S(q)$ versus the product of q and aggregate radius of gyration R_g, representing a dimensionless form of the probing length. Fig. 5 shows that size-delimited power-law regimes exist in the $S(q)$ trend. First, a fractal regime, with a slope ($-D_f$) taking value between -2.2 and -2.6, can be observed within the length scale $1 < qR_g < 10$. As qR_g further increases, a kink point is reached, beyond which $S(q)$ takes up a steeper trend with a slope ($-2D_m + D_s$) of -4. This second power-law regime ($qR_g > 10$) is also known as Porod regime, wherein the probing length is below average monomer radius and consequentially the aggregates are seen as 3-d Euclidian objects (i.e. $D_m = 3$ and $D_s = 2$) [44].

One could observe that the reconstructed soot aggregates have $2.2 < D_f < 2.6$, which are noticeably larger than the $D_f \approx 1.8$ of the DLCA aggregates. Qualitatively speaking, this is in good agreement with the visual appearances of our ET reconstructed aggregates, which manifest more compact morphology than that of the idealized DLCA aggregates. Specifically, significant degrees of inter-monomer necking can be observed in the ET reconstructions, which obfuscate the point-contacting arrangement of monomers typically assumed in DLCA. Furthermore, the possible restructuring of aggregate backbone (as indicated by the internal ring structure in aggregate C), could also lead to a more compact packing arrangement for monomers.

4.3. Optical properties

Since spherical particles are widely used in regional climate models, in this section, we calculate the optical properties of spherical particles using Mie theory with reference to the two aggregate models mentioned in previous sections. The material of soot aggregates considered in this study is isotropic black carbon, so the polarizability tensor α_j degrades to a scalar quantity [46].

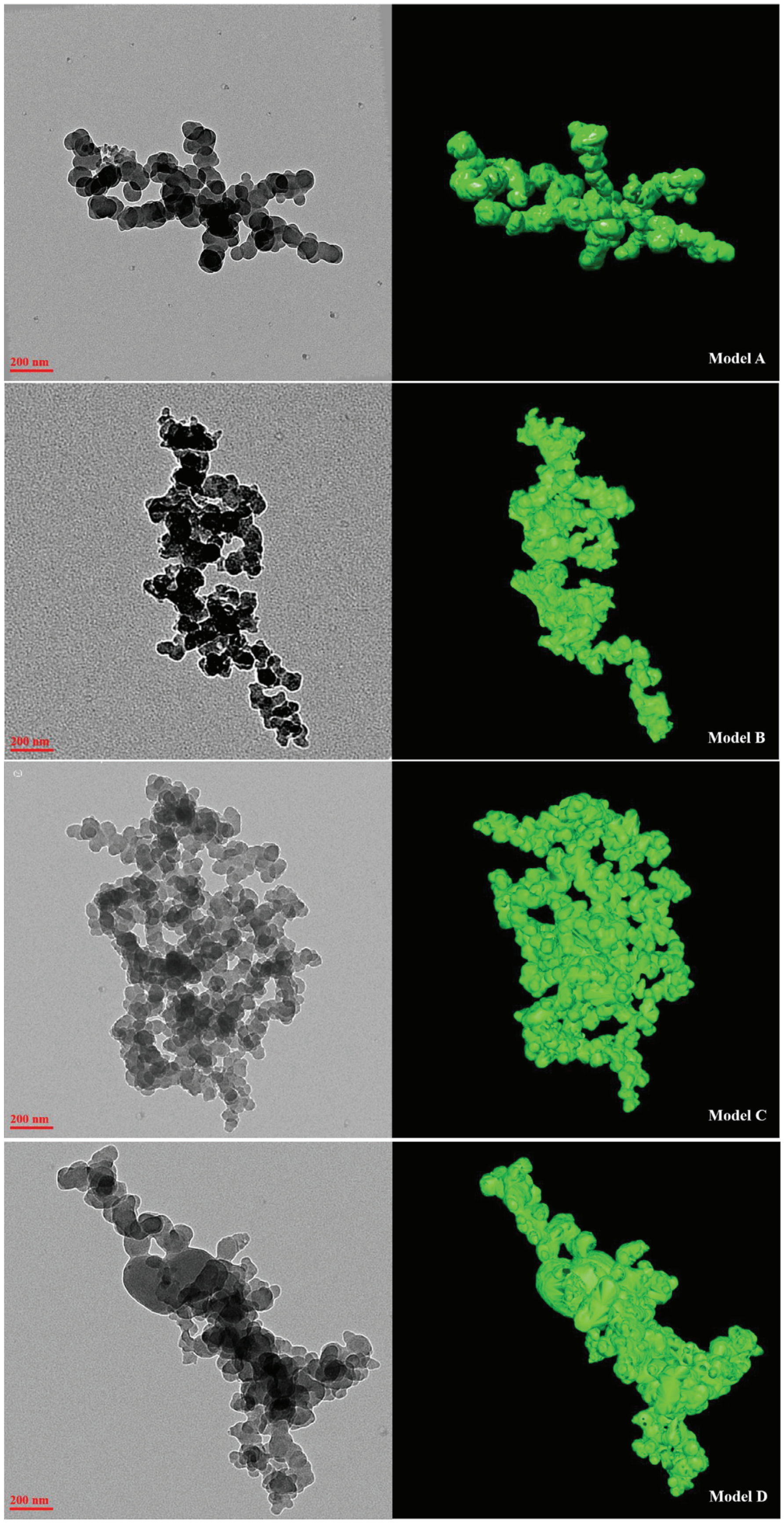

Fig. 4. Electron Tomography reconstruction of aggregates A, B, C, and D. The left panels show the transmission EM images of the soot aggregates. The right panels show the 3-d reconstructed geometries of the corresponding aggregates.

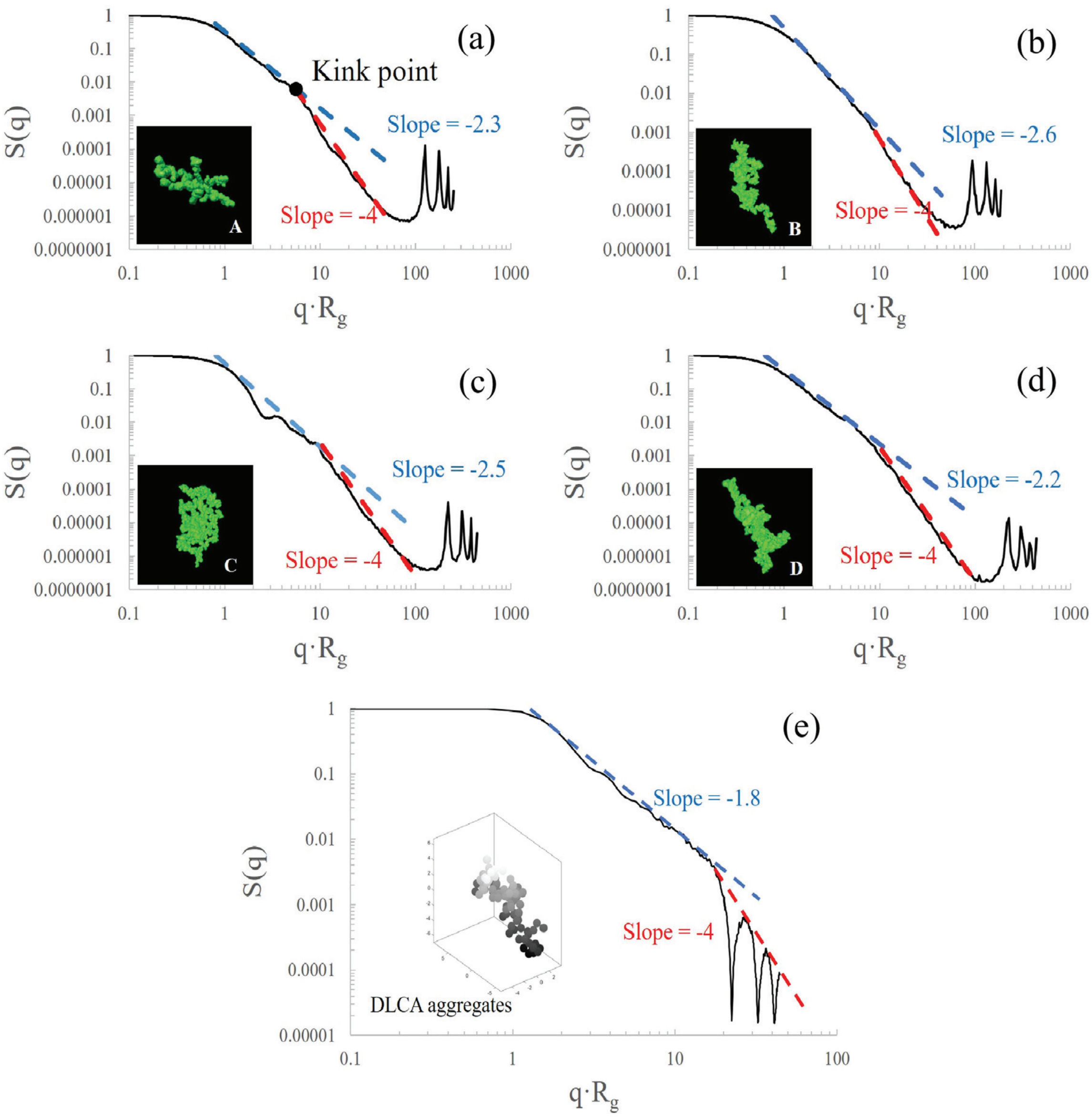

Fig. 5. Panels (a) - (d) Q-space analysis of four ET aggregates, Panel (e) Q-space analysis of a typical DLCA aggregate

First, we choose a moderate refractive index, 1.95-0.79i [47], as the typical refractive index of black carbon to study the effects of different particle morphologies to their optical properties. At the end of this section, we will provide a sensitivity analysis of aggregates' optical properties to different refractive indices.

Fig. 6 (a) and (b) respectively show the single scattering albedo (SSA) and asymmetric factor of ET reconstructed aggregates as functions of incident light wavelength. Also plotted here are the SSA and asymmetric factor determined from DLCA model and the volumetrically equivalent spheres. In Fig. 6 (a), the black cross symbols represent the mean value of SSA calculated using the four ET reconstructed aggregates. (Detailed optical properties of ET reconstructed aggregates are shown in Table S1). Blue circle symbols represent the statistical SSA of DLCA aggregates with different number of primary particles, which have volumetrically equivalent radii between 0.27 μm to 0.40 μm. The red circle symbols represent the SSA calculated for volumetrically equivalent spheres with Mie theory. The styles of symbol in Fig. 6 (b) follows that in (a).

The values of SSA and the asymmetry parameter are observed to decrease with an increase in the incident wavelength. This observation holds true for both the ET reconstructed aggregates and the idealized models (i.e. DLCA and spherical particles). Specifically, the use of DLCA model results in a systematic underestimation of SSA; whereas overestimated SSA values are observed in the case of equivalent spherical model. This observation implies that when the aggregate morphology becomes less compact, the contribution of scattering to total extinction tends to decrease. Meanwhile, both DLCA and the equivalent spherical particle model systematically underestimate the values of asymmetry parameter. This observation indicates that the underestimated asymmetric parameter cannot be deterministically related with the compactness of aggregate morphology. Future studies should focus on elucidating the sensitivity of asymmetric parameters on other non-ideal minor structures of aggregates.

Fig. 7 shows the mass absorption cross section (MAC), along with the absorption angstrom exponent (AAE) values, calculated from the ET reconstructed aggregates, DLCA aggregates, and equivalent spherical model. MAC in this study is defined as:

$$MAC = \frac{Q_{abs} \cdot \pi r_{equ}^2}{\frac{4}{3}\rho \pi r_{equ}^3}, \quad (4)$$

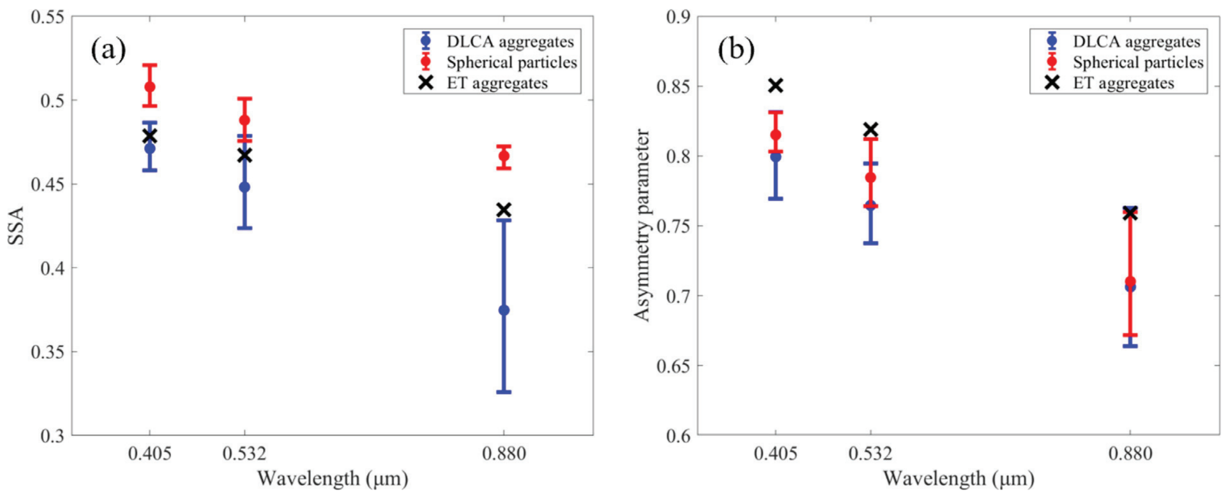

Fig. 6. Single scattering albedos (a) and asymmetry parameter (b) of ET reconstructed aggregates, DLCA aggregates, and volumetrically equivalent sphere with radii ranging from 0.27 μm to 0.40 μm.

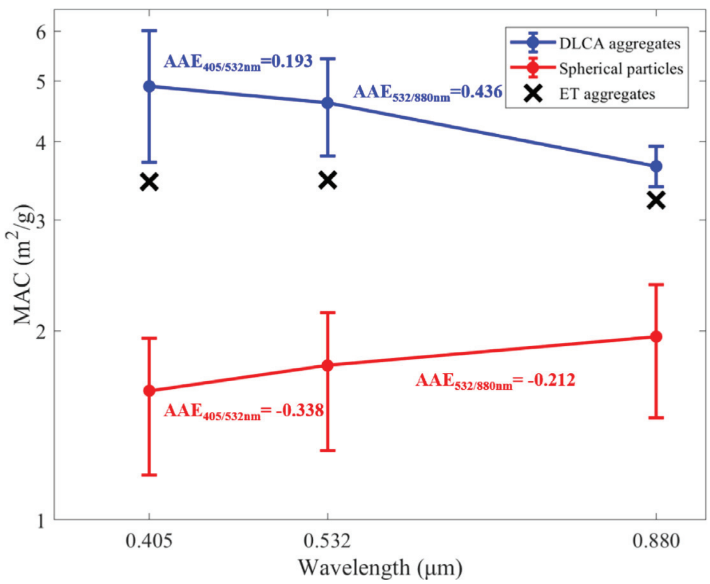

Fig. 7. Wavelength dependence of Mass Absorption Cross-sections (MAC) for ET soot aggregates, and comparison with equivalent DLCA soot aggregates and volumetrically equivalent soot spheres. As is apparent, MAC values of ET aggregates are spectrally invariant.

Here, Q_{abs} is the orientational averaged absorption efficiency of an aggregate, r_{equ} is the volumetrically equivalent radius of the aggregate, and ρ is its density. The average MAC of ET aggregates is 35.6%, 27.8%, and 9.7% lower than the DLCA counterparts with comparable size and monomer numbers, and is 54.2%, 50.1%, and 40.6% higher than their volumetrically equivalent spheres at 405 nm, 532 nm, and 880nm, respectively. We estimate the average MAC of ET aggregates, based on an assumption of black carbon's density of 1.8 g/cm^3, to be ~3.43 m^2/g at 532 nm. Our observation of three different particle models implies that aggregates with less compact morphologies are greater light absorbers, even without any coating. No significant wavelength dependency is observed for the MAC of the ET reconstructed aggregates; whereas a slightly positive AAE is observed for comparable DLCA aggregates, and a negative value is observed for that of the equivalent spherical models. According to Rayleigh-Debye-Gans (RDG) theory, particles with diameters smaller than the wavelength and with a moderate refractive index have an absorption efficiency written as:

$$Q_{abs} = -\frac{4x}{3}\mathrm{Im}\left(m^2 - 1\right), \quad (5)$$

Here, x is the size parameter (product of particle radius and the wavenumber of incident light), and m is the complex refractive index. Since m is assumed to be wavelength independent, $AAE = -\ln(MAC_{\lambda_1}/MAC_{\lambda_2})/\ln(\lambda_1/\lambda_2)$ by its definition is close to a constant value of unity [48,49]. Figure S3 plots AAE values as functions of volumetrically equivalent radii for spherical particles derived from Mie theory. As particle radii increase, AAE values of both wavelength pairs rise above constant one and dramatically decrease below zero. In our study, the volumetrically equivalent radii of all aggregate models are larger than 0.27 μm. If we define the spherical particles sharing comparable AAE values to the aggregated particles as "AAE-equivalent spheres", the size of AAE equivalent spheres (shaded in grey in Figure S3) of the ET reconstructed aggregate is smaller than that of the volumetrically equivalent spheres (shaded in red in Figure S3).

Previous studies quantified the influence of fractal morphologies on absorption using the concept of phase-shift parameter [44,50]. The "optical effective radius" significantly decreases after it is corrected to account for the small packing fraction of fractal aggregates. Our results (in Fig. 7 and Figure S3) validate the fractal

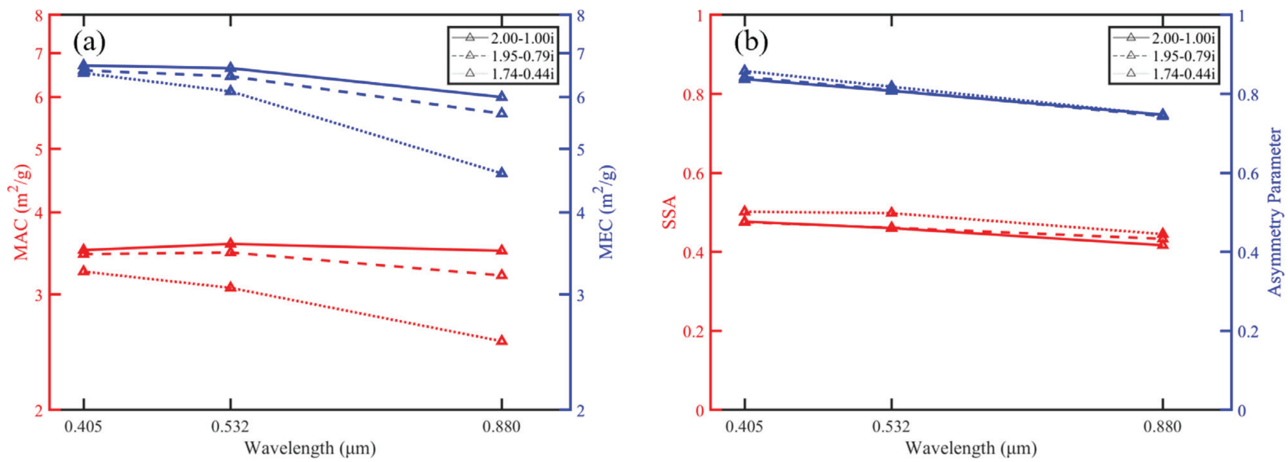

Fig. 8. Variation in mass absorption (MAC) and extinction cross sections (MEC), single scattering albedo (SSA) and asymmetry parameter of ET aggregates as a function of varying refractive indices. The plots show the sensitivity of optical properties to varying values of complex refractive index.

morphologies lead to a deviation between geometric and optical equivalent size.

In Fig. 8, we evaluate how different refractive indices affect ET aggregate optical properties. Besides $m = 1.95 - 0.79i$, two published values, $2.00 - 1.00i$ [51] and $1.74 - 0.44i$ [52] are applied to show the sensitivities of previously mentioned optical properties. MEC in Fig. 8 (a) represents the mass extinction cross section. It is similarly defined as MAC in Eq. (4) but substitutes extinction efficiency Q_{ext} for Q_{abs}. We found higher m values amplify particle extinction and absorption cross-sections. Meanwhile, the characteristic of wavelength independent AAE has been preserved under two high m value assumptions. For $m = 1.74 - 0.44i$, a weak inverse wavelength dependence of MAC is observed. Fig. 8 (b) shows that SSA and asymmetry parameters are less sensitive to variations in refractive indices.

5. Conclusion

We apply electron tomography coupled with a slice-by-slice voxel filling algorithm to reconstruct the 3-d morphology of soot aggregates sampled from a coal combustion system. The non-ideal structure of soot aggregates (i.e. non-spherical monomers, necking structures between monomers, and the internal rings structures), which are rarely considered in computer simulation, have been accurately preserved in the ET reconstruction. The morphology and optical properties of the soot aggregates are respectively studied with DDA and q-space analysis, which are directly applied to the ET reconstruction. Structure factor obtained from q-space analysis proves to be effective in quantitating the size delimited aggregate morphology. The D_f of the ET reconstructed aggregates takes values in the range between 2.2 and 2.6, indicating more compact morphologies than that of the idealized DLCA aggregates. The optical properties of ET reconstructed aggregates are compared with that of the idealized DLCA aggregates and volumetrically equivalent spheres. Our results show that the fractal-like morphology leads to enhancements in both the magnitude of MAC and the fraction of absorption in total extinction. The MAC of spherical particles is observed to have a weak dependency on incident wavelength, parameterized with a negative AAE value, when their size parameters slightly exceed unity; Whereas the MAC of ET aggregates remains constant with changing incident wavelengths, this wavelength independence holds for high refractive index values. Moreover, no deterministic relationship has been observed between the asymmetric parameter and the compactness of the aggregate morphology. Future works should be directed towards understanding the influence of the non-ideal structure of real-world aggregates on their asymmetric parameter. We should emphasize that our findings here are based on single particle analysis, which therefore could deviate from the ensemble qualities of soot particles suspended in atmosphere.

Declaration of Competing Interest

The authors declare that they have no known competing financial interests or personal relationships that could have appeared to influence the work reported in this paper.

Acknowledgments

The authors thank Ulugbek Kamilov and Xiaojian Xu in Department of Computer Science and Engineering at Washington University in St. Louis, and Hongwei Wang, Xueming Li, and Anbao Jia in the School of Life Sciences at Tsinghua University for providing computing facilities for the ET reconstruction work. The authors also appreciate Wenhua Wang, Siyi Cai, and Jie Li for their assistance in soot sampling experiment. This work was partially-made possible by the generous funding support from the McDonnell International Scholars Academy, US National Science Foundation (AGS-1455215 and AGS-1926817), and the National Key R & D Program of China.

Supplementary materials

Supplementary material associated with this article can be found, in the online version, at doi:10.1016/j.jqsrt.2020.107184.

References

[1] Kanagawa M, Nakata T. Analysis of the energy access improvement and its socio-economic impacts in rural areas of developing countries. Ecol Econ 2007;62:319–29.

[2] Li Q, Jiang JK, Wang SX, Rumchev K, Mead-Hunter R, Morawska L, et al. Impacts of household coal and biomass combustion on indoor and ambient air quality in China: current status and implication. Sci Total Environ 2017;576:347–61.

[3] Yao CS, Chen CY, Li M. Analysis of rural residential energy consumption and corresponding carbon emissions in China. Energ Policy 2012;41:445–50.

[4] Rosen H, Hansen ADA, Dod RL, Novakov T. Soot in urban atmospheres - determination by an optical-absorption technique. Science 1980;208:741–4.

[5] Wornat MJ, Ledesma EB, Sandrowitz AK, Roth MJ, Dawsey SM, Qiao YL, et al. Polycyclic aromatic hydrocarbons identified in soot extracts from domestic goal burning stoves of Henan Province, China. Environ Sci Technol 2001;35:1943–52.

[6] Rogelj J, Schaeffer M, Meinshausen M, Shindell DT, Hare W, Klimont Z, et al. Disentangling the effects of CO2 and short-lived climate forcer mitigation. P Natl Acad Sci USA 2014;111:16325–30.

[7] Sand M, Berntsen TK, von Salzen K, Flanner MG, Langner J, Victor DG. Response of Arctic temperature to changes in emissions of short-lived climate forcers. Nat Clim Change 2016;6:286.
[8] Cai J, Lu N, Sorensen CM. Comparison of size and morphology of soot aggregates as determined by light-scattering and electron-microscope analysis. Langmuir 1993;9:2861–7.
[9] Liu L, Mishchenko MI, Arnott WP. A study of radiative properties of fractal soot aggregates using the superposition T-matrix method. J Quant Spectrosc Ra 2008;109:2656–63.
[10] Tian K, Thomson KA, Liu FS, Snelling DR, Smallwood GJ, Wang DS. Determination of the morphology of soot aggregates using the relative optical density method for the analysis of TEM images. Combust Flame 2006;144:782–91.
[11] Wentzel M, Gorzawski H, Naumann KH, Saathoff H, Weinbruch S. Transmission electron microscopical and aerosol dynamical characterization of soot aerosols. J Aerosol Sci 2003;34:1347–70.
[12] Orhan O, Haffner-Staton E, La Rocca A, Fay M. Characterisation of flame–generated soot and soot-in-oil using electron tomography volume reconstructions and comparison with traditional 2D-TEM measurements. Tribol Int 2016;104:272–84.
[13] Wozniak M, Onofri FRA, Barbosa S, Yon J, Mroczka J. Comparison of methods to derive morphological parameters of multi-fractal samples of particle aggregates from TEM images. J Aerosol Sci 2012;47:12–26.
[14] Chakrabarty RK, Moosmuller H, Arnott WP, Garro MA, Tian GX, Slowik JG, et al. Low fractal dimension cluster-dilute soot aggregates from a premixed flame. Phys Rev Lett 2009:102.
[15] Heinson WR, Sorensen CM, Chakrabarti A. Does shape anisotropy control the fractal dimension in diffusion-limited cluster-cluster aggregation? Aerosol Sci Tech 2010:44 I-Iv.
[16] Brasil AM, Farias TL, Carvalho MG. A recipe for image characterization of fractal-like aggregates. J Aerosol Sci 1999;30:1379–89.
[17] Chakrabarty RK, Garro MA, Garro BA, Chancellor S, Moosmuller H, Herald CM. Simulation of aggregates with point-contacting monomers in the cluster-dilute regime. part 2: comparison of two- and three-dimensional structural properties as a function of fractal dimension. Aerosol Sci Tech 2011;45:903–8.
[18] Baldelli A, Trivanovic U, Rogak SN. Electron tomography of soot for validation of 2D image processing and observation of new structural features (vol 53, pg 575, 2019). Aerosol Sci Tech 2019:53 I-I.
[19] Vanheel M. Angular reconstitution - a posteriori assignment of projection directions for 3-D reconstruction. Ultramicroscopy 1987;21:111–23.
[20] Asnaghi D, Carpineti M, Giglio M, Sozzi M. Coagulation kinetics and aggregate morphology in the intermediate regimes between diffusion-limited and reaction-limited cluster aggregation. Phys Rev A 1992;45:1018–23.
[21] Weitz DA, Huang JS, Lin MY, Sung J. Dynamics of diffusion-limited kinetic aggregation. Phys Rev Lett 1984;53:1657–60.
[22] Heinson WR, Sorensen CM, Chakrabarti A. A three parameter description of the structure of diffusion limited cluster fractal aggregates. J Colloid Interf Sci 2012;375:65–9.
[23] Teng SW, Liu C, Schnaiter M, Chakrabarty RK, Liu FS. Accounting for the effects of nonideal minor structures on the optical properties of black carbon aerosols. Atmos Chem Phys 2019;19:2917–31.
[24] Kim AS, Yuan R. Cake resistance of aggregates formed in the diffusion-limited-cluster-aggregation (DLCA) regime. J Membrane Sci 2006;286:260–8.
[25] Meakin P. Formation of fractal clusters and networks by irreversible diffusion-limited aggregation. Phys Rev Lett 1983;51:1119–22.
[26] Al Zaitone B, Schmid HJ, Peukert W. Simulation of structure and mobility of aggregates formed by simultaneous coagulation, sintering and surface growth. J Aerosol Sci 2009;40:950–64.
[27] Balthasar M, Frenklach M. Monte-Carlo simulation of soot particle coagulation and aggregation: the effect of a realistic size distribution. P Combust Inst 2005;30:1467–75.
[28] Eggersdorfer ML, Pratsinis SE. The structure of agglomerates consisting of polydisperse particles. Aerosol Sci Tech 2012;46:347–53.
[29] Li CH, Kattawar GW, Yang P. Effects of surface roughness on light scattering by small particles. J Quant Spectrosc Ra 2004;89:123–31.
[30] Adachi K, Chung SH, Friedrich H, Buseck PR. Fractal parameters of individual soot particles determined using electron tomography: Implications for optical properties. J Geophys Res-Atmos 2007:112.
[31] van Poppel LH, Friedrich H, Spinsby J, Chung SH, Seinfeld JH, Buseck PR. Electron tomography of nanoparticle clusters: Implications for atmospheric lifetimes and radiative forcing of soot. Geophys Res Lett 2005:32.
[32] Sorensen CM. Q-space analysis of scattering by particles: a review. J Quant Spectrosc Ra 2013;131:3–12.
[33] Draine BT, Flatau PJ. Discrete-dipole approximation for scattering calculations. J Opt Soc Am A 1994;11:1491–9.
[34] Draine BT, Flatau PJ. Discrete-dipole approximation for periodic targets: theory and tests. J Opt Soc Am A 2008;25:2693–703.
[35] Arslan I, Tong JR, Midgley PA. Reducing the missing wedge: High--resolution dual axis tomography of inorganic materials. Ultramicroscopy 2006;106:994–1000.
[36] Goris B, Van den Broek W, Batenburg KJ, Mezerji HH, Bals S. Electron tomography based on a total variation minimization reconstruction technique. Ultramicroscopy 2012;113:120–30.
[37] Heinson WR, Liu P, Chakrabarty RK. Fractal scaling of coated soot aggregates. Aerosol Sci Tech 2017;51:12–19.
[38] Flatau PJ, Draine BT. Light scattering by hexagonal columns in the discrete dipole approximation. Opt Express 2014;22:21834–46.
[39] Li Q, Jiang JK, Cai SY, Zhou W, Wang SX, Duan L, et al. Gaseous ammonia emissions from coal and biomass combustion in household stoves with different combustion efficiencies. Environ Sci Tech Let 2016;3:98–103.
[40] Wang WH, Shao LY, Li J, Chang LL, Zhang DZ, Zhang CC, et al. Characteristics of individual particles emitted from an experimental burning chamber with coal from the lung cancer area of Xuanwei, China. Aerosol Air Qual Res 2019;19:355–63.
[41] Amat F, Moussavi F, Comolli LR, Elidan G, Downing KH, Horowitz M. Markov random field based automatic image alignment for electron tomography. J Struct Biol 2008;161:260–75.
[42] Kremer JR, Mastronarde DN, McIntosh JR. Computer visualization of three-dimensional image data using IMOD. J Struct Biol 1996;116:71–6.
[43] Heinson YW, Maughan JB, Heinson WR, Chakrabarti A, Sorensen CM. Light scattering Q-space analysis of irregularly shaped particles. J Geophys Res-Atmos 2016;121:682–91.
[44] Sorensen CM. Light scattering by fractal aggregates: A review. Aerosol Sci Tech 2001;35:648–87.
[45] Schnitzler EG, Dutt A, Charbonneau AM, Olfert JS, Jager W. Soot aggregate restructuring due to coatings of secondary organic aerosol derived from aromatic precursors. Environ Sci Technol 2014;48:14309–16.
[46] Draine BT, Flatau PJ. User guide for the discrete dipole approximation code DDSCAT 7.3. arXiv preprint arXiv:13056497. 2013.
[47] Bond TC, Bergstrom RW. Light absorption by carbonaceous particles: an investigative review. Aerosol Sci Tech 2006;40:27–67.
[48] Bohren CF, Huffman DR. Absorption and scattering of light by small particles: John Wiley & Sons; 2008.
[49] Rayleigh On the scattering of light by a cloud of similar small particles of any shape and oriented at random. Philos Mag 1918;35:373–81.
[50] Chakrabarty RK, Heinson WR. Scaling laws for light absorption enhancement due to nonrefractory coating of atmospheric black carbon aerosol. Phys Rev Lett 2018:121.
[51] Donnet J-B. Carbon black: science and technology. CRC Press; 1993.
[52] Jaenicke R. Atmospheric aerosols and global climate. Climatic variations and variability: facts and theories: springer; 1981. p. 577-97.